remote sensing

MDPI

Article

Assessing the Impact of Tides and Atmospheric Fronts on Submesoscale Physical and Bio-Optical Distributions near a Coastal Convergence Zone

Richard W. Gould Jr. [1,*], Stephanie Anderson [1], M. David Lewis [1], W. David Miller [2], Igor Shulman [1], Geoffrey B. Smith [2], Travis A. Smith [1], David W. Wang [1] and Hemantha W. Wijesekera [1]

[1] Ocean Sciences Division, US Naval Research Laboratory, Code 7300, Stennis Space Center, MS 39529, USA; stephanie.anderson@nrlssc.navy.mil (S.A.); david.lewis@nrlssc.navy.mil (M.D.L.); igor.shulman@nrlssc.navy.mil (I.S.); travis.smith@nrlssc.navy.mil (T.A.S.); david.wang@nrlssc.navy.mil (D.W.W.); hemantha.wijesekera@nrlssc.navy.mil (H.W.W.)

[2] Remote Sensing Division, US Naval Research Laboratory, Code 7200, Washington, DC 20375, USA; dave.miller@nrl.navy.mil (W.D.M.); geoffrey.smith@nrl.navy.mil (G.B.S.)

* Correspondence: richard.gould@nrlssc.navy.mil; Tel.: +1-228-688-5587

Received: 14 November 2019; Accepted: 5 February 2020; Published: 7 February 2020

Abstract: Optically-active constituents vary over short time and space scales in coastal waters, and they are impacted by a variety of complex, inter-related forcing processes. As part of the Integrated Coastal Bio-Optical Dynamics (ICoBOD) project, we conducted a field campaign in Mississippi Sound in the northern Gulf of Mexico during spring 2018 to examine the impact of the passage of atmospheric and tidal fronts on fine-scale physical and bio-optical property distributions in a shallow, dynamic, coastal environment. During a 25-day experiment, we deployed eight moorings over a roughly 7 × 7 km box encompassing a frontal zone, to collect a time series of physical and bio-optical measurements. We describe changes in diver visibility related to the passage of a short-duration, high-turbidity surface plume and nepheloid layer development/decay during a tidal cycle. Maximum nepheloid layer development was observed during low tide and lasted about 9–12 h. The strongest turbidity signal extended about 4–5 m above the bottom (approximately half of the water column), although anomalously elevated values were observed all the way to the surface. In addition, high-resolution (50 m) hydrodynamic model simulations provide insight into the frontal dynamics and aid interpretation of the observed patterns. Mooring observations confirmed model-predicted heat flux changes associated with the passage of an atmospheric cold front.

Keywords: coastal; bio-optics; hydrodynamic modeling; remote sensing; circulation; currents; tides; winds; bio-physical interactions; time series

1. Introduction

Optically active constituents (OACs) in water, both dissolved and particulate, and the water itself, attenuate light through absorption and scattering processes and thereby control the intensity and spectral quality of the penetrating light [1,2]. OACs include phytoplankton, detritus, sediments, and colored dissolved organic matter (CDOM). The intensity and spectral quality of the penetrating light in turn impact the OACs, for example, through the regulation of primary production (and thus the abundance and species composition of the phytoplankton) [3,4] and the photobleaching of CDOM [5,6]. Thus, there is a feedback between the ambient light field and the OACs, with one impacting the other. The inherent optical properties (IOPs) of the water, such as absorption and scattering coefficients, depend only on the medium itself, through the concentration and composition of

OACs. IOPs are the properties often measured with bio-optical instrumentation, as in this study, often in conjunction with measurement of biogeochemical properties, such as chlorophyll and suspended sediment concentrations. In contrast, the apparent optical properties (AOPs), such as remote sensing reflectance (R_{rs}) and the diffuse attenuation coefficient (K_d), depend on both the OACs and the ambient light field. Satellite estimates of Rrs are commonly used in bio-optical inversion algorithms to retrieve the water IOPs [7].

Light penetration also impacts a wide variety of navy operations related to active/passive electro-optical (EO) sensor performance, underwater target detection/identification, diver visibility, vulnerability of subsurface vehicles, and hydrodynamic modeling (through heat flux modulation). Thus, it is important to understand bio-optical variability and the processes that impact that variability, particularly in dynamic coastal areas where bio-optical properties can vary over several orders of magnitude over very short space and time scales due to interacting biological, chemical, and physical processes [8–10]. In coastal waters, the concentration and distribution of OACs are controlled by a complex interaction of physical and biological processes related to: discharge plumes of dissolved organic matter associated with river effluent, resuspension of bottom sediments, nutrient-stimulated phytoplankton blooms, meteorological conditions, and advection by strong local currents [11,12].

Two physical processes play a key role in controlling the variability of coastal circulation: wind forcing associated with the passage of atmospheric fronts, and tidal currents. The coastal circulation in turn drives the OAC distributions (and thus the bio-optical properties), to a large extent. Thus, to better characterize the bio-optical patterns, our goal is to understand the driving processes and their interaction. Atmospheric frontal passages, typically associated with stronger surface winds, occur regularly in the Gulf of Mexico, on average every 5–8 days from late fall to spring [13]; these fronts serve to periodically mix the water column and alter the distribution of OACs, and thus bio-optical properties. This mixing effect is exacerbated in shallow coastal zones and lakes where the wind-induced wave action can penetrate to the seafloor, leading to resuspension of bottom sediments and detritus throughout a shallow water column [14–16], or confined in high scattering/absorbing nepheloid layers near the bottom [17]. During extreme storm events, such as a hurricane, wind-driven bottom nepheloid layers have even been observed in the deep sea, extending up to 200 m above the seafloor at a water depth of 1500 m [18]. The ebb and flow of tidal currents can also lead to nepheloid layer development [19] and to the development of surface convergence zones that can potentially "trap" dissolved and particulate materials, particularly in regions of strong density gradients [20,21]. Depending on the co-occurrence, intensity, and timing of the atmospheric and tidal fronts, they can combine to reinforce or ameliorate the convergence zones. Thus, atmospheric and tidal fronts further complicate an already complex coastal bio-optical picture, although the intensity, extent, and duration of the bio-optical alterations they impart are poorly known.

Modeling advances are enabling development of high-resolution coupled ocean/atmosphere models for coastal waters. Recent advances in the air/ocean/wave Coupled Ocean/Atmosphere Mesoscale Prediction System (COAMPS, [22–24]) to support coastal modeling include a wetting and drying routine, additional coastal wave breaking physics, and utilization of very high-resolution bathymetry (3 arc-sec or less). For the first time, we have pushed the COAMPS model temperature, salinity, and current fields to 50 m horizontal resolution (see Section 2.2 for further model details). The model results can help us understand the atmospheric and hydrodynamic mechanisms driving the physical and bio-optical property distributions, with the caveat that the models must first be adequately validated. So, although this is not a model validation paper per se, we do address model/data comparisons to a limited extent (through a comparison between mooring temperatures and model heat flux simulations associated with the passage of an atmospheric cold front), to give confidence in the model results. Additional model validation and more detailed model results will be presented elsewhere (Smith et al., in preparation).

Remote sensing from a range of platforms can provide the opportunity to measure coastal processes over broad spatial and temporal scales. For example, traditional ocean color sensors such

as the Moderate Resolution Imaging Spectroradiometer (MODIS) and the Visible/Infrared Imaging Radiometer Suite (VIIRS) are both multispectral with limited spectral coverage over visible wavelengths (seven and six channels, respectively) and provide only coarse spatial resolution imagery (1 km and 750 m, respectively). These sensors have the benefit that they operate continuously with global coverage; together, they can provide between one and three overpasses per day over a given location (VIIRS collects an image of a given area at least once a day, sometimes twice if the orbits overlap, and MODIS collects an image every day, or every other day). Imagery from the Landsat-8 and WorldView-3 satellites, while still multispectral, provides much higher spatial resolution (30m and 2–4m, respectively), but with a limited repeat cycle (16 days for Landsat). In addition, tasking costs can be high (for WorldView). Spectroradiometers deployed on aircraft or unmanned aerial vehicles (UAV) can provide even finer spatial resolution imagery (meter-to-sub-meter scale), and with finer spectral resolution (roughly 5 nm, measured contiguously over the entire visible/near-infrared spectrum from 400 to 900 nm). Aircraft and UAV sensors provide much greater flexibility in sampling frequency and coverage, although deployment costs for aircraft can be high, and both sensor types generally operate over fairly limited periods (the duration of a field program, for instance). During the field campaign for the Integrated Coastal Bio-Optical Dynamics (ICoBOD) project, we collected hyperspectral visible and thermal aircraft imagery at 1 m resolution at roughly 6-minute intervals for several hours, and hyperspectral UAV imagery at cm-scale resolution. High spectral/spatial/temporal resolution remote sensing imagery from a combination of sensors can provide unprecedented views of coastal ocean processes.

Although synoptic surface remote sensing imagery using a suite of satellite, aircraft, and UAV sensors at multiple spatial resolutions can provide detailed horizontal coverage, it provides no depth information. Ship sampling can provide vertical profiles, and continuous, underway surface mapping can extend the horizontal coverage. However, fine-scale temporal variability is generally lacking, unless the ship sits on station and collects frequent repeat casts at a single location. Moorings, with either a profiling capability or with instruments at fixed depths in the water column, provide continuous temporal measurements of the vertical structure of the water column, albeit at a limited number of locations. By combining remote sensing imagery with ship and mooring data, we can better link the surface and subsurface distributions with the temporal variability. The mooring time series are continuous, whereas the imagery was collected less frequently, at discrete times. Thus, the mooring data can fill temporal gaps, by providing information at times when there is no imagery, at least at a few fixed locations. In turn, the imagery can help extend the mooring time series spatially, by providing context on the broader surface horizontal distributions.

The main goals of the ICoBOD project are to: (1) assess how advection, diffusion, and bottom resuspension associated with these two key forcing processes affect bio-optical distributions at multiple time scales in shallow coastal areas, and (2) develop empirical relationships between bio-optical, physical, and atmospheric properties. Such relationships can help describe the dependence of the bio-optical distributions (magnitude and temporal variability) on factors such as wind speed, water depth, waves, and sediment type, and will allow prediction of optical properties from measured or modeled physical properties. We examine variability at time scales from minutes to weeks, and spatial scales from sub-meter to kilometers. Here, we present an overview of the field experiment, methods, in situ data collection, environmental conditions during the field work, remote sensing imagery, and the modeling approach. We also highlight several key results related to the variability of coastal diver visibility, nepheloid layer development/decay during a tidal cycle, and surface heat flux simulations associated with the passage of an atmospheric cold front. Additional analyses are underway to better understand frontal dynamics (using model simulations and remote sensing imagery to track dye mixing) and coupled physical/bio-optical variability (using the mooring time series).

2. Methods and Data

The field work was conducted in March–April 2018 in a shallow barrier island environment in the northern Gulf of Mexico. Previous surface current data (2001) collected with a Coastal Ocean Dynamics Applications RADAR (CODAR) system indicated the development of regular, persistent tidal convergence fronts near the pass between Ship and Horn Islands in Mississippi Sound in the northern Gulf of Mexico. Tides in this region are predominately diurnal. These islands are located about 16 km south of Biloxi Bay, Mississippi, with water depths of 4–6 m inside the Sound and 10–11 m outside. Surface fronts were observed in the CODAR data during ebb tide on days with a coincident southerly wind (i.e., when winds and tides opposed) and lasted 5–8 h (Figure 1a); during ebb tide on days with northerly winds, fronts were not observed (i.e., winds and tides reinforced) (Figure 1b). Furthermore, measured current fields have shown the development of daily tidal fronts and two-layer vertical structure, even in this shallow "presumably" well-mixed area, and a few bio-optical profiles have shown the presence of a bottom nepheloid layer (J. Book, R. Gould, unpublished data).

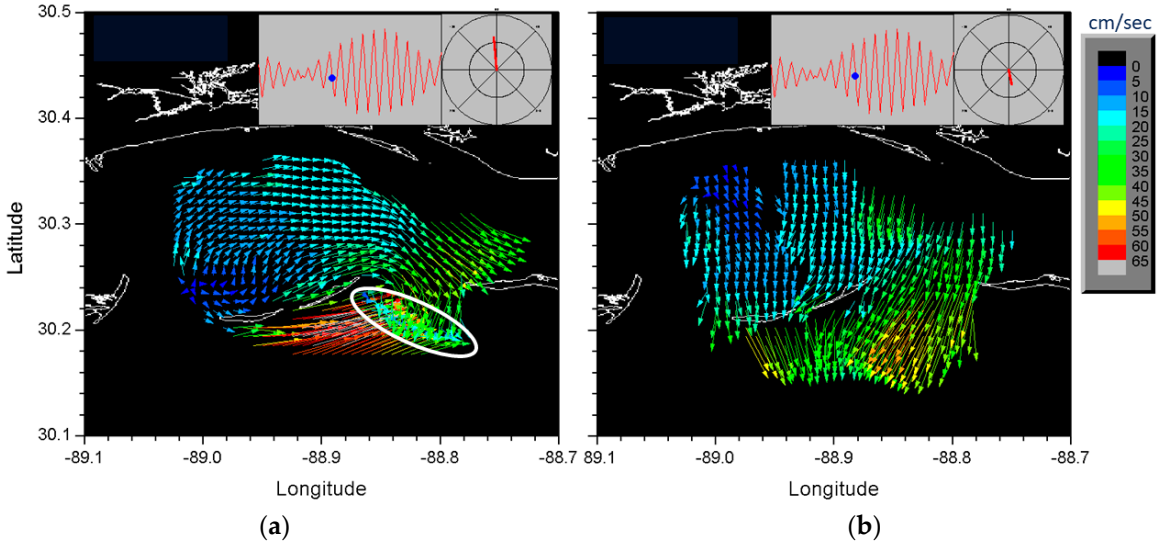

Figure 1. Coastal Ocean Dynamics Application RADAR (CODAR) surface currents in Mississippi Sound, south of Biloxi Bay, Mississippi Sound. Blue dot in top panel of each figure indicates the tidal stage corresponding to the currents. Wind rose in the right panel indicates wind direction. (**a**) Ebb flow, southerly wind (winds and tides oppose; front is observed, white oval); (**b**) Ebb flow, northerly wind (winds and tides reinforce; no front).

Thus, by selecting this region for study we increased the likelihood of success of observing the development and dissipation of coastal fronts, as related to tides and variable north/south winds associated with the passage of atmospheric cold fronts. The field work was planned for a time of year when cold fronts still routinely pass through our area of interest in Mississippi Sound (based on a wind climatology). Our goal was to encompass two spring/neap tidal cycles, water column mixing during the passage of atmospheric cold fronts, and quiescent periods prior to and following passage of the cold fronts, to quantify the horizontal and vertical time evolution of the associated bio-optical perturbations (magnitude, extent). We were fortunate to capture the passage of four cold fronts during the 25-day period our moorings were deployed. Cold fronts with strong northerly winds occurred starting around 3/30, 4/4, 4/8, and 4/15 and lasted approximately 1–3 days until winds switched back around to the south. The environmental conditions are shown in Figure 2.

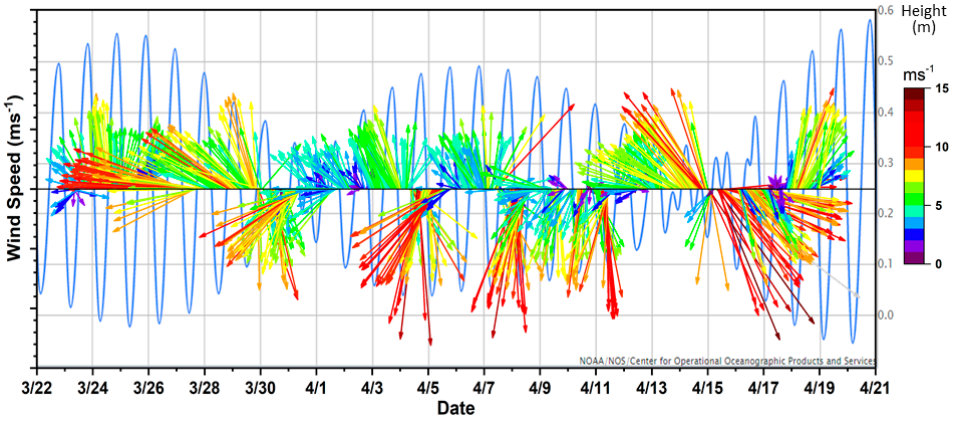

Figure 2. Environmental conditions during the Integrated Coastal Bio-Optical Dynamics ICoBOD field work in 2018. Tidal stage shown in blue (height in m, right axis) with wind vectors overlaid (length and color indicate wind speed, ms^{-1}).

2.1. In Situ Data

Using the R/V Point Sur (operated by the University of Southern Mississippi), we deployed eight moorings on 3/24 and 3/25 in the area of the convergence front observed in the prior CODAR data, and recovered seven of them on 4/16 and 4/17 (one mooring, LM2, was lost at sea). We selected the mooring locations to encompass the northern and southern range of variability in the observed front location. The moorings were deployed in three east/west oriented lines, with the northernmost line of 3 moorings deployed just shoreward of the pass, the middle line of 2 moorings deployed roughly in the center of the pass, and the southernmost line of 3 moorings deployed just seaward of the pass. The moorings were spaced about 3.5 km apart along each line, and the three mooring lines were separated by about 3.5 km as well (thus, they covered an area of roughly 7 × 7 km). The moorings provided time series of physical and bio-optical properties in and around the pass between Ship and Horn Islands in Mississippi Sound, south of Biloxi, MS. The mooring locations are shown in Figure 3. Our study area is a shallow area subject to strong wave and current conditions. It is also heavily-trafficked by both recreational and commercial vessels, and thus represents a risky area to deploy moored instruments.

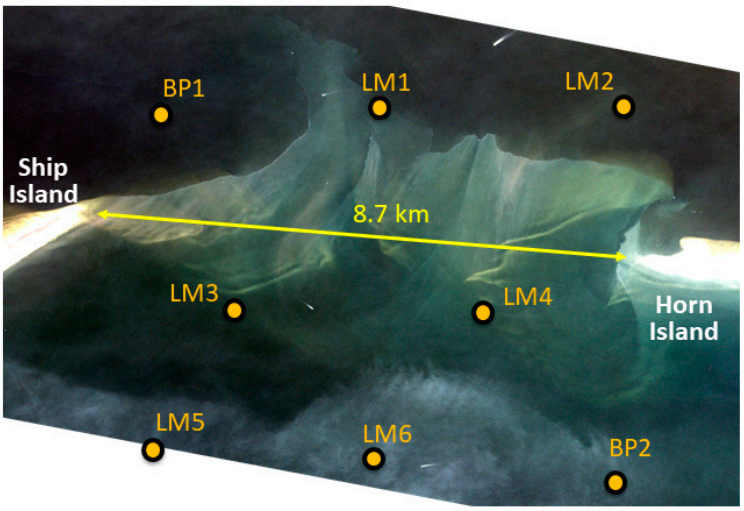

Figure 3. Mooring locations in Mississippi Sound, between Ship and Horn Islands. The background is a true color Planet nanosatellite image collected at 1600 UTC on 3/25/2018.

Six of the moorings were line moorings, each consisting of two bio-optical/physical sensor packages (near-surface and near-bottom nodes). Teledyne/RDI Acoustic Doppler Current Profilers (ADCP) were

located at two of the line mooring sites. Another mooring consisted of just a bottom ADCP and a surface Seabird Conductivity, Temperature, Depth (CTD) sensor (no optics). The final mooring was a Bio-Optical/Physical Pop-up Environmental Reconnaissance System (BOPPERS, at location BP2 in Figure 3), which consists of a trawl-resistant bottom housing containing an ADCP and a profiling unit that deploys at regularly scheduled intervals (every 3 h in this case) to sample the entire water column [25]. The trawl-resistant base allows for deployment in areas with routine commercial fishing operations; following the profile, the profiling unit is winched back into the base and stored until the next cast, to reduce exposure risk in the water column. However, upon recovery, we found that the line for the profiling unit had been cut (perhaps by an engine propeller) and the profiler was gone, so the CTD and optical instruments contained within were lost as well. The BOPPERS bottom base unit and instrumentation (including the ADCP) was successfully recovered. Thus, the BOPPERS CTD and optical records were shorter than the full deployment time (profile records only from 3/24 to 3/27). Furthermore, when we returned to recover mooring LM2, it was completely gone, so no data were recovered from that location.

Physical instrumentation included Seabird microcat SBE37 CTDs on the string moorings and a Seabird SBE 52MP CTD on the BOPPERS. Nortek bottom ADCPs were located with four of the moorings. Optical instrumentation included Turner C6Ps with sensors for turbidity, chlorophyll, colored dissolved organic matter (CDOM), uranine, and rhodamine fluorescence. Each sensor was calibrated in the lab with standards of known concentration prior to deployment. The C6P instruments sampled every 3 minutes and were equipped with a wiper mechanism to clean the optical windows prior to each sample, to reduce bio-fouling. SeaBird optical instrumentation included a Beam Attenuation Meter (BAM, 657 nm), ECO bb3 backscattering sensors (470, 532, 650 nm), ECO FL3 fluorescence sensors (chlorophyll, CDOM, rhodamine), a downwelling irradiance sensor OCR507 (412, 443, 490, 532, 555, 670 nm, PAR), and an ac9 sensor to measure absorption and beam attenuation (412, 440, 488, 510, 532, 555, 650, 676, 715 nm). Time-lapse, panchromatic video cameras (Brinno TLC200 Pro) enclosed in waterproof pressure cases collected frames every 20 seconds at the surface and bottom nodes of moorings LM1 and LM5. The instrumentation on each mooring is listed in Table 1.

Table 1. Mooring locations and instrumentation. Water depths at mooring location are indicated in parentheses. BP2 was a profiling mooring (thus, no surface or bottom instrument nodes), the others were line moorings. See text for further clarifications and parameters measured. CTD: Conductivity, Temperature, Depth; C6P: 6-channel fluorometer; ECO FL3: Environmental Characterization Optics 3-channel fluorometer; ECO bb3: 3-channel backscatter sensor; BAM: Beam Attenuation Meter; OCR 507: Ocean Color Radiometer, 7-channels.

Mooring	Latitude	Longitude	Near Surface	Near Bottom	Bottom ADCP
LM1 (6.1 m)	30°15.982′	−88°49.474′	C6P, CTD, ac9, ECO bb3, ECO FL3, camera	C6P, CTD, camera	
LM2 (6.0 m)	30°16.013′	−88°47.185′	lost at sea		
LM3 (6.0 m)	30°13.992′	−88°50.811′	C6P, CTD	C6P, CTD	600 kHz, 2 min sampling, 0.5 m vertical resolution, wave pack
LM4 (7.6 m)	30°14.010′	−88°48.467′	C6P, CTD	C6P, CTD	
LM5 (11.1 m)	30°12.632′	−88°51.538′	C6P, CTD, camera	C6P, CTD, camera	500 kHz 5-beam, 20 min sampling, 0.5 m vertical resolution, wave pack
LM6 (10.8 m)	30°12.572′	−88°49.497′	C6P, CTD	CTD	
BP1 (6.8 m)	30°15.887′	−88°51.532′	CTD		1000 kHz 5-beam, 20 min sampling, 0.25 m vertical resolution, wave pack
BP2 (11.3 m)	30°12.455′	−88°47.147′	Profiler: CTD, BAM, OCR 507, ECO bb3, ECO FL3		1200 kHz, 2 min sampling, 0.25 m vertical resolution, wave pack

2.2. Modeling

High-resolution (50 m) 3-dimensional hydrodynamic model simulations were performed to provide a dynamical understanding of the coastal frontal processes, and to help us better understand the processes driving the bio-optical distributions, by separating the effects of tides and atmospheric forcing on the bio-optical property distributions. The Coupled Ocean/Atmosphere Mesoscale Prediction System (COAMPS) couples an atmospheric model with hydrodynamic and wave models to make both mesoscale and microscale predictions of the atmosphere and ocean [22–24,26]. COAMPS includes a globally relocatable grid, user-defined grid resolutions and dimensions, nested grids, and an option for idealized or real-time simulations.

The atmospheric model within COAMPS consists of a complete 3-dimensional variational (3DVAR) data assimilation system with data quality control, analysis, initialization, and forecast model components through the NRL Atmospheric Variational Data Assimilation System (NAVDAS) [27]. The hydrodynamic model is the Navy Coastal Ocean Model, (NCOM) [28] and the wave model can be either the Simulating WAves Nearshore (SWAN) [29] or WaveWatch III model [30]. The coupling between the models is accomplished through the Earth System Modeling Framework (ESMF) [31]. In the fully-coupled mode, COAMPS, NCOM, and SWAN (or WaveWatch III) can be integrated concurrently so that precipitation and surface fluxes of moisture and momentum are exchanged across the air–sea interface. Waves are not simulated in this study, but may be added in future work.

COAMPS model simulations for the Mississippi Bight and ICoBOD observational area were completed for March-April 2018. The COAMPS model setup for ICoBOD consisted of an atmospheric domain with 18, 6, and 2 km horizontal atmospheric resolution nests and 60 terrain-following vertical levels. The 2 km atmospheric nest provided forcing for 125 m and 50 m NCOM ocean nests. Atmospheric boundary conditions were provided by the Navy Global Environmental Model (NAVGEM) [32]). The atmospheric model was run in 24-h cycles beginning at 00 UTC each day. At the beginning of each cycle, data assimilation is initiated by NAVDAS using the prior 24-h forecast as background, incorporating quality-controlled observations from radiosondes, aircraft, satellite, ship, and surface stations. Daily atmospheric assimilation cycles enable COAMPS to properly position atmospheric fronts to more accurately depict the surface winds that drive the oceanic circulation.

The NCOM configuration consisted of two nests (125 m and 50 m resolution) that encompassed the ICoBOD area of interest in the northern Gulf of Mexico. The model domains are shown in Figure 4. A total of 50 vertical levels are utilized, 36 of which are sigma coordinate levels in the upper 500 m of the water column for each of the nests. The bathymetry was derived from the NOAA 3-second (90 m) Coastal Relief Model (CRM, https://www.ngdc.noaa.gov/mgg/coastal/crm.html) data set. Initial and boundary conditions for NCOM are typically derived from The Fleet Numerical Meteorology and Oceanography Center (FNMOC) Global Hybrid Coordinate Ocean Model (HYCOM) [33]. Observational and global ocean data, including quality-controlled satellite, ship, profiler, and Modular Ocean Data Assimilation System (MODAS) [34] synthetic profile data for each 24-h update cycle, are ingested through the 3DVAR Navy Coupled Ocean Data Assimilation system (NCODA) [35]. The 125 m nest boundary conditions were derived from a 1 km resolution Gulf of Mexico run that is run daily in-house at NRL, while the 50 m nest boundary conditions were derived from the 125 m nest simulation. Tides were included in the boundary conditions from the 1 km Gulf of Mexico run and both nests utilized river flows. Each COAMPS simulation was run at the Navy DoD Supercomputing Resource Center (Navy DSRC).

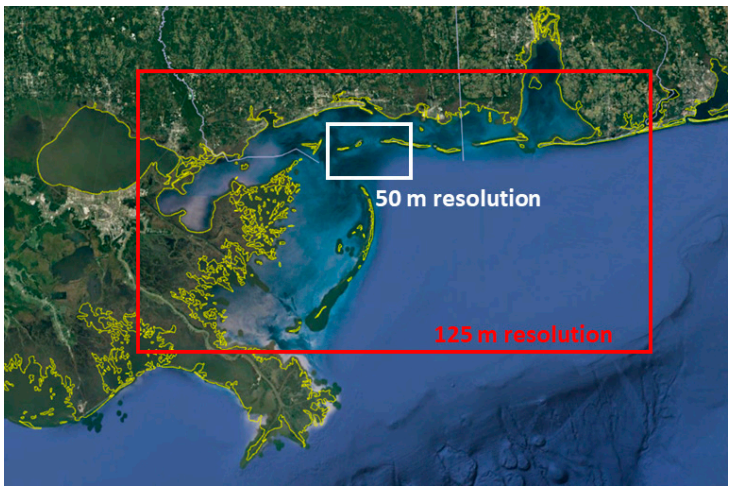

Figure 4. Coupled ocean–atmosphere model domains, northern Gulf of Mexico (outer nest: 125 m resolution, inner nest: 50 m resolution).

3. Results

3.1. Mooring Results—Turbidity/Diver Visibility

The turbidity time series from the near-surface sensor at mooring LM1 is shown in Figure 5a. Large turbidity peaks are evident near the beginning of the time series on 3/27 (associated with strong southeasterly winds), and near the end of the time series on 4/15 (associated with a cold front and strong northerly winds, see Figure 2). Similar turbidity maxima at those times were also observed at all of the other moorings (data not shown). These were periods of increased wave heights, so the turbidity maxima were likely due to wave-generated bottom resuspension that mixed throughout the water column all the way to the surface (bottom resuspension does not always reach the surface, however, it can be confined in a nepheloid layer close to the bottom, as we present later).

Notice the brief (2-h duration), sharp turbidity spike on 3/29 (highlighted by the red box in Figure 5a), which we will examine in more detail below. A corresponding turbidity spike was not observed at the bottom sensor at LM1 (data not shown), so it is unlikely that it was due to bottom resuspension, and the a-periodic nature of the spike suggests it was unrelated to tidal forcing. Thus, it was probably associated with an advected surface plume.

To assess changes in diver visibility associated with the turbidity variability, we first calculated horizontal diver visibility (HDV, in meters) from the beam attenuation coefficient at 532 nm [36]:

$$\mathrm{HDV} = 4.55/[0.9 * \mathrm{c}(532) + 0.081], \quad (1)$$

Turbidity measurements were collected at multiple surface and bottom sensors on the line moorings. However, as indicated above, the optics-to-diver visibility relationship requires an estimate of the beam attenuation coefficient, which was available at only one mooring location (LM1). In order to estimate diver visibility at the other locations, we needed to develop an estimate of c(532) from turbidity, so we first merged the near-surface CTD and bio-optical data (temperature, salinity, turbidity, chlorophyll, colored dissolved organic matter (CDOM) concentration, beam attenuation, and absorption coefficients) from the SeaBird and Turner sensors at mooring LM1. Based on those measurements, we then developed a robust relationship between turbidity and the beam attenuation coefficient:

$$\mathrm{c}(532) = 0.78038 * \mathrm{turbidity} + 1.67585, \quad (2)$$

where c(532) units are m^{-1} and turbidity units are NTU. This least-squares linear regression is shown in Figure 5b (R^2 = 0.96). When coupled with Equation (1), it enables us to estimate horizontal diver visibility at all the remaining mooring locations that had turbidity measurements.

We also mounted underwater time-lapse, panchromatic video cameras adjacent to several of the sensor packages (see Table 1), and we matched up individual camera frames captured during the short, high-turbidity pulse highlighted in Figure 5a to the optical measurements. This provides an underwater visualization of the impact of optical changes (water turbidity) on diver visibility. The times indicated in Figure 6a correspond to the camera frames and associated horizontal diver visibility ranges shown in Figure 6b (the camera was mounted at the top of the instrument cage pointing downward; the distance from the camera face to the bottom of the cage was about 0.6 m).

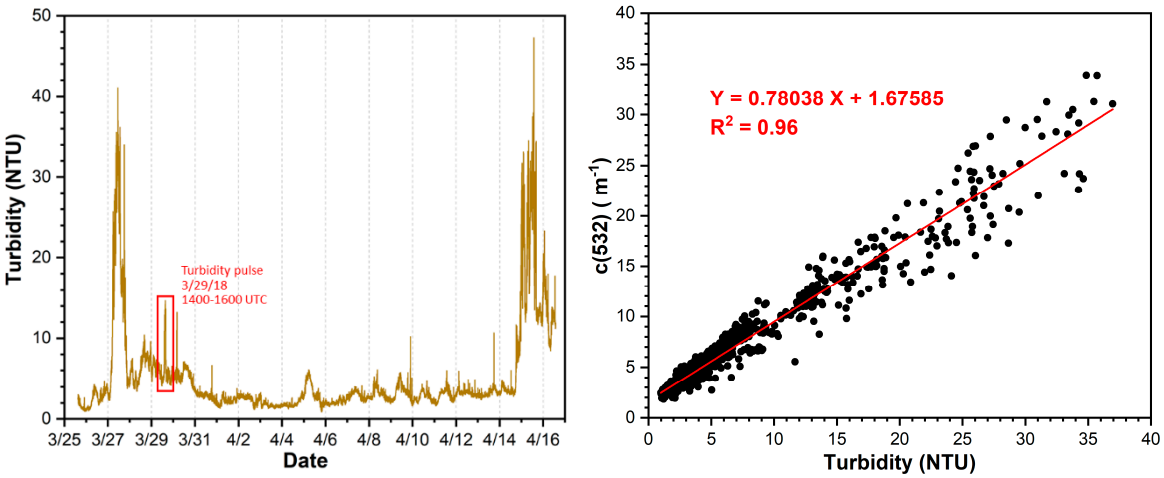

Figure 5. (**a**) Turbidity time series from mooring LM1, surface node. The red box indicates the 2-h turbidity pulse shown in more detail in Figure 6; (**b**) Beam attenuation coefficient at 532 nm, c(532), vs. turbidity. Red line and equation depict the least-squares linear regression best-fit, and coefficient of determination, R^2.

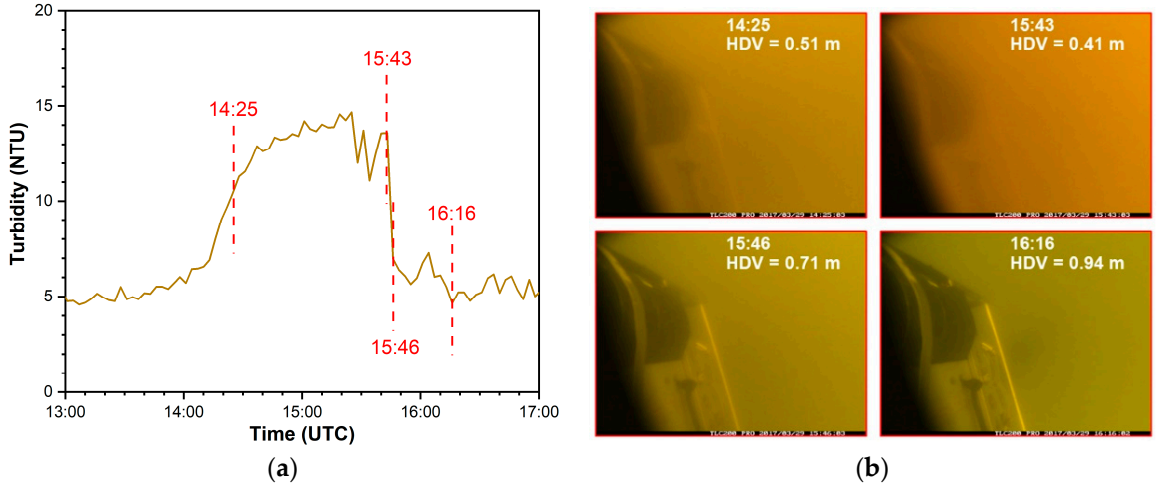

Figure 6. (**a**) Turbidity from mooring LM1, 13:00–1700 UTC on 3/29; (**b**) Underwater camera frames corresponding to times indicated in **a**. Horizontal diver visibility calculated from c(532) is indicated on each frame.

Near the beginning of the turbidity spike at 14:25, a turbidity value of 9.8 corresponds to an HDV value of 0.51 m. Near the peak of the pulse at 15:43, the increase in turbidity has decreased the HDV to 0.41 m. At the next turbidity measurement 3 minutes later, turbidity has decreased roughly in half and

HDV has increased to 0.71 m. After the pulse has passed, 30 min later (at 16:16) the turbidity is back to background levels with HDV of 0.94 m. Visually, this image looks very similar to pre-pulse images (not shown).

3.2. Mooring Results—Physical Properties

Example time series of temperature, salinity, and density, from the top and bottom nodes at one mooring (LM3) are shown in Figure 7. Note the warm, low salinity pulse observed at the surface node from about 16:00 UTC on 4/3–09:00 UTC on 4/4 (depicted by the black oval in Figure 7a), associated with southerly winds (Figure 2). A precipitous decrease in temperature and increase in salinity followed this pulse, related to the tidal currents and the passage of a cold front (see further discussion below in Sections 3.4 and 4). Although the pulse is also observed at the bottom node, it is shorter and less intense, and seems to be split into two distinct features (Figure 7b). There is less high-frequency variability observed at the bottom node compared to the top node; this is also true for density (Figure 7c). There are clear instances of two-layer structure evident at times in the density record (large differences in the surface and bottom densities), even at this shallow location (6 m), as well as instances of a well-mixed water column (similar surface and bottom densities). We have similar data sets at the other mooring sites, which will enable similar surface vs. bottom and inter-site comparisons.

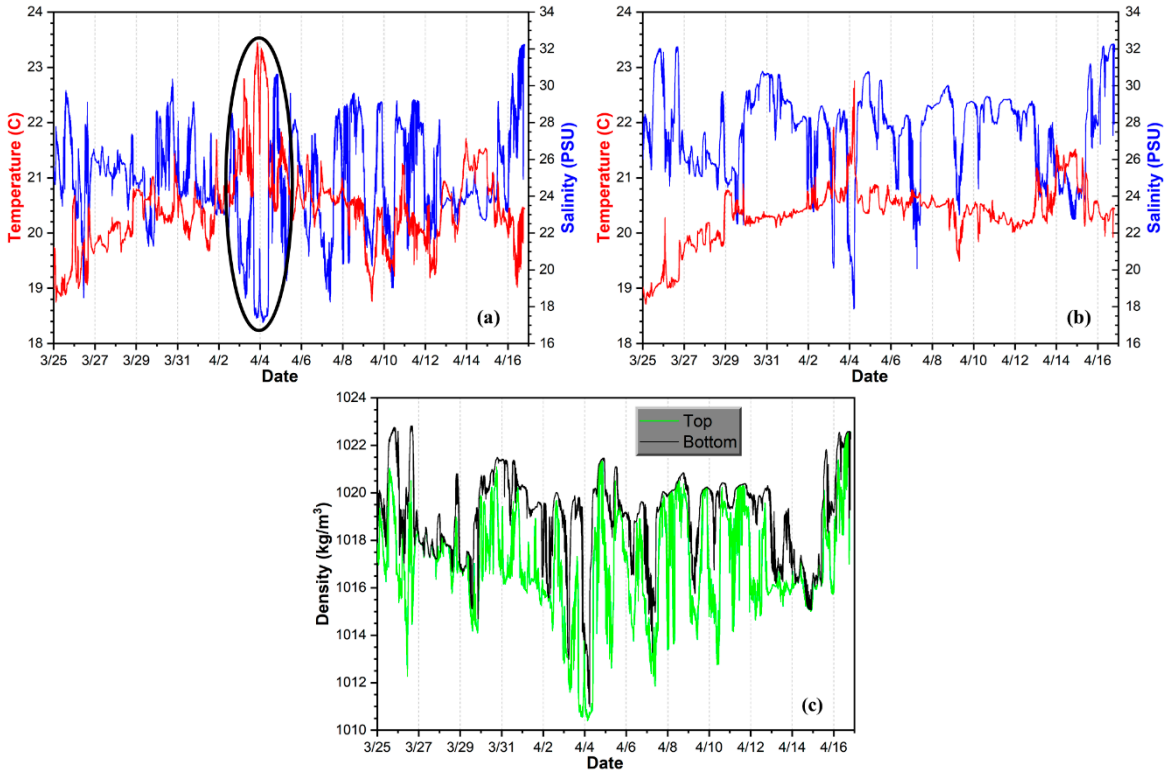

Figure 7. (**a**) Temperature and salinity, LM3 top (black oval denotes a warm, low salinity pulse followed by a temperature decrease and a salinity increase, as described in the text); (**b**) Temperature and salinity, LM3 bottom; (**c**) Density, LM3, top and bottom.

We have processed the data from the four ADCPs to provide water current speeds and directions at the four individual sites. Currents from mooring LM5 are shown in Figure 8 (includes tides). We use these data to assess water column baroclinicity and vertical shear, as well as small-scale spatial variability of the currents across the study region. In this region, diurnal tides are the main tidal component, with a similar frequency to the inertial currents. As in the density record, we observe baroclinic, 2-layer structure even at these shallow water depths, with strong vertical shear. Although currents in general are fairly weak in this record (0.5 m/s and less), the east-west currents (U component)

are somewhat stronger than the north-south currents (V component). High-frequency variability is observed, particularly around periods of stronger winds, for example on 4/4, 4/5, 4/15, and 4/17, during the passage of cold fronts. We have performed spatial averages of the ADCP data (upper 2 m and bottom 2 m of the water column) to facilitate comparisons with the data sets from the near-surface and near bottom physical and bio-optical sensor packages. We are also comparing the spatially- and temporally-averaged ADCP and model current data sets, to determine how well the model results capture the observed patterns. The depth-averaged model and in situ ADCP currents agree closely in phase, and in magnitude (current speeds) in the north–south direction, but agreement in the east–west direction is weaker (data not shown). Model validation aspects will be presented in greater detail in Smith et al. (in preparation).

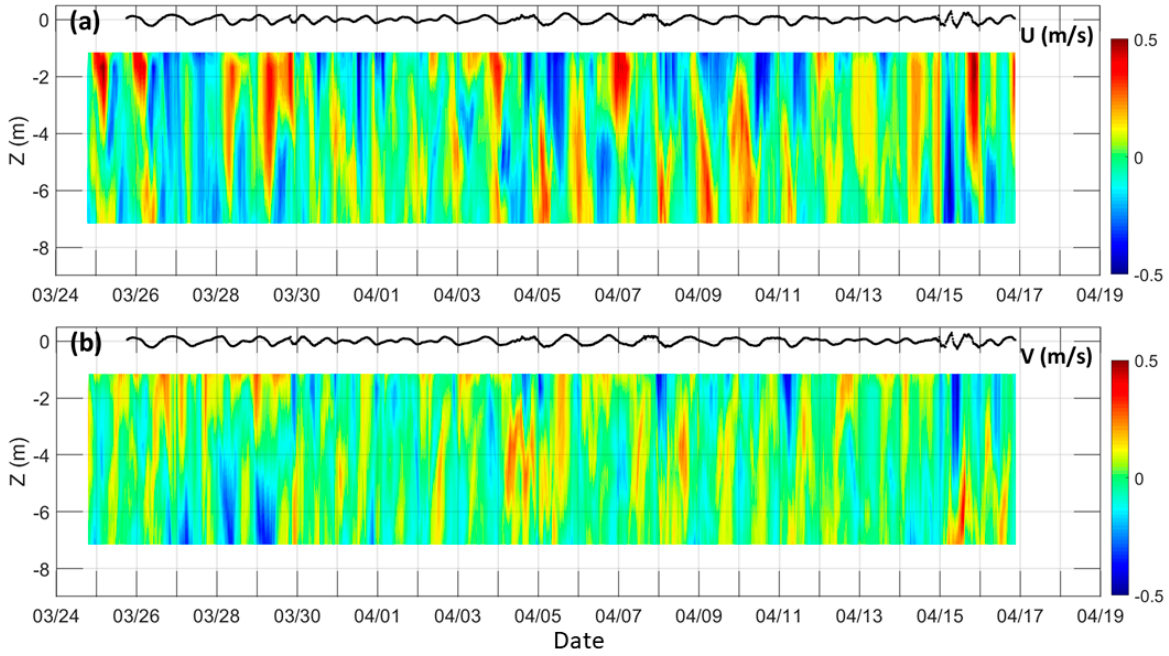

Figure 8. Time series of Acoustic Doppler Current Profiler (ADCP) currents from mooring LM5. (**a**) U component (flow toward the east positive); (**b**) V component (flow toward the north positive). Black lines at the top of each panel indicate water height.

Significant wave heights derived from surface-tracking wave parameter data at the four ADCP mooring locations are shown in Figure 9. There were two periods of higher waves during the deployment period that correspond to periods of higher turbidity on 3/27 and 4/15 (Figure 5a), suggesting the waves extended to the seafloor and led to sediment resuspension. Wave heights at the southern moorings (LM5, BP2) exceeded those at the more northward (shoreward) moorings (LM3, BP1). Significant wave heights typically decrease moving from offshore to onshore, under similar wind conditions.

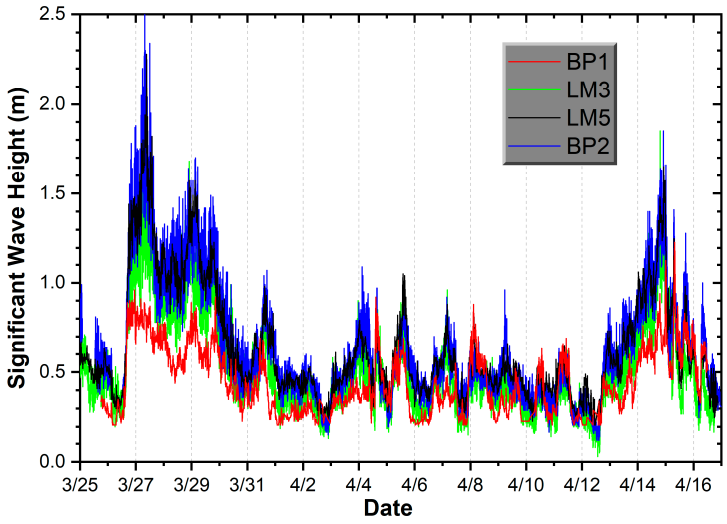

Figure 9. Significant wave heights during ICoBOD field work, at the four mooring locations with ADCP sensors.

3.3. Nepheloid Layer Development/Decay

Although only a single BOPPERS unit was deployed (BP2, at 10m water depth just seaward toward the southeast of the Ship/Horn Island pass) and the data record was truncated (only 4 days long, due to instrument loss), it collected ADCP current data coincidently with water column physical/bio-optical profiles collected every 3 h. The temperature, salinity, and beam attenuation coefficient are shown in Figure 10. Note that although the bottom temperature shows only minimal temporal variability, larger periodic salinity and beam attenuation (turbidity) pulses are observed in the bottom 4 m of the water column (related to the tides). Visual inspection of Figure 10b,c shows similar patterns; the higher salinity values (>33.5 PSU) correspond to the higher attenuation values (>7.5 m^{-1}). This indicates periodic development and decay of a bottom nepheloid layer related to the tidal currents, with the layer lasting about 9–12 h. The highest turbidity portion of the layer extended up about 4–5 m from the bottom, although anomalously high values (above background levels) reached the surface (Figure 10c). Note also the correspondence between the c(657) and echosounder data, indicating that the echo intensity data can be used as an indicator of turbidity in the nepheloid layer [37].

On 3/26 a mixing event is observed in the temperature, salinity, and c(657) records around noon (Figure 10a–c). There were weak south winds (2–3 m/s) until 10:00; after that, speeds increased to 10–11 m/s from the east-southeast. This mixed the warmer, lower salinity, lower turbidity surface water downward, and resulted in a completely well-mixed water column from the surface to the bottom in about 3 h (between 12:00 and 15:00, the time of the next cast).

Corresponding ADCP currents at BP2 are shown in Figure 11, with water height (tidal stage) derived from the ADCP pressure sensor indicated at the top of each panel. Based on the c(657) and echo intensity records in Figure 10c, nepheloid layer development started around 21:00 on 3/24 (with maximum turbidity levels then lasting about 12 h), and around 00:00 on 3/26 (with maximum levels lasting about 9 h). The layer development coincides with a reversal of currents from east to west and from south to north, representing slack tide prior to flood stage. The bottom turbidity levels at BP2 during the field work between 4/2 and 4/6 (as indicated by the echo intensity data) indicate similar patterns with maximum turbidity levels and nepheloid layer development observed during low tide, and lowest turbidity levels observed during high tide (Figure 12). This pattern was disrupted on 4/4 and 4/5, likely due to bottom resuspension associated with the strong north winds during the cold front passage (see Figure 2). The turbidity pattern re-established by 4/6.

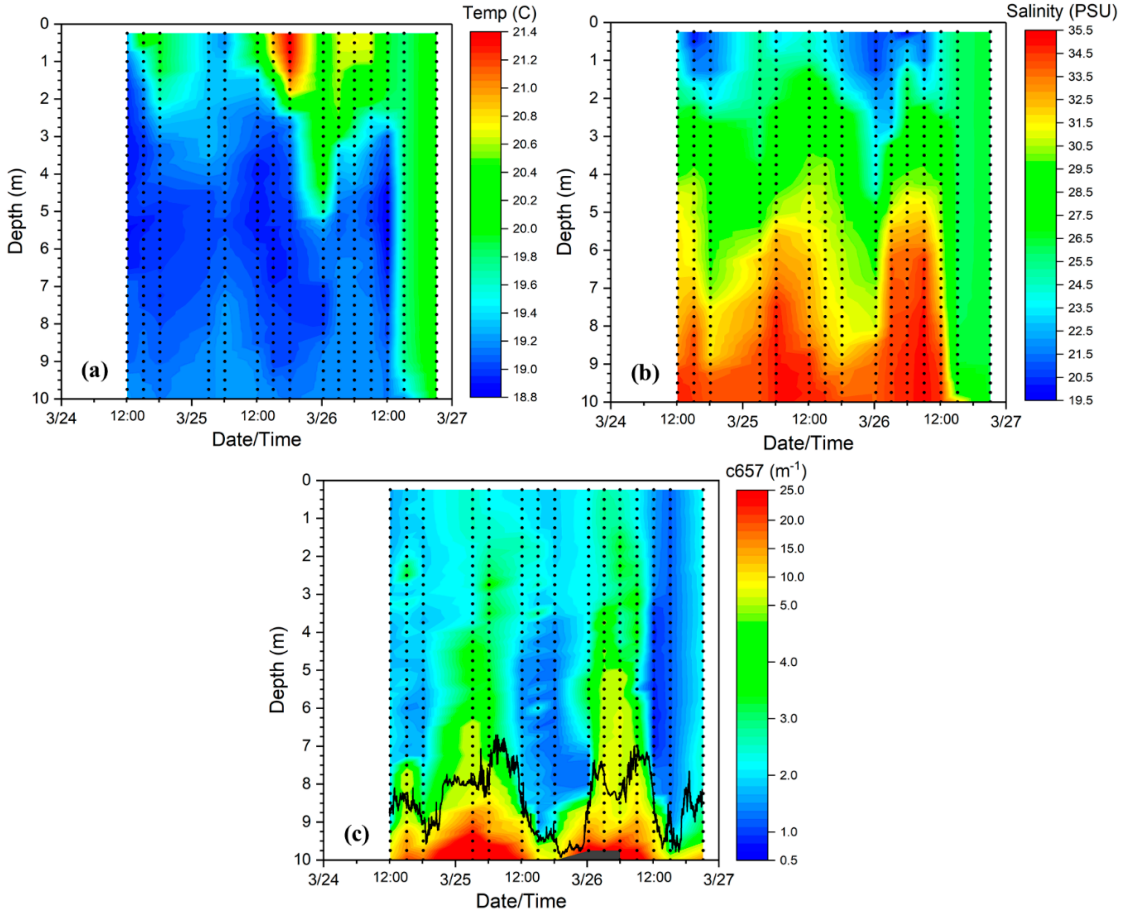

Figure 10. Vertically-resolved time series from mooring BP2 (profiling mooring). The black dots represent the spatial (vertical) and temporal sampling resolution. (**a**) Temperature; (**b**) Salinity; (**c**) Beam attenuation coefficient, c(657). The black line indicates echo intensity data from the ADCP (arbitrary scale). Times indicated are local (UTC—5 h).

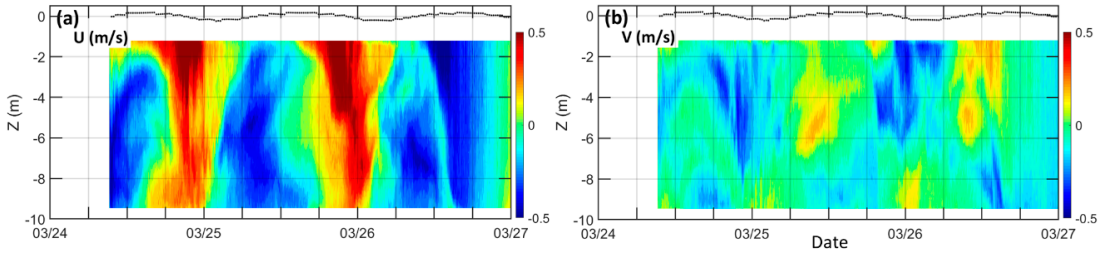

Figure 11. Time series of ADCP currents from mooring BP2. (**a**) U component (flow toward the east positive); (**b**) V component (flow toward the north positive). Times indicated are local (UTC—5 h).

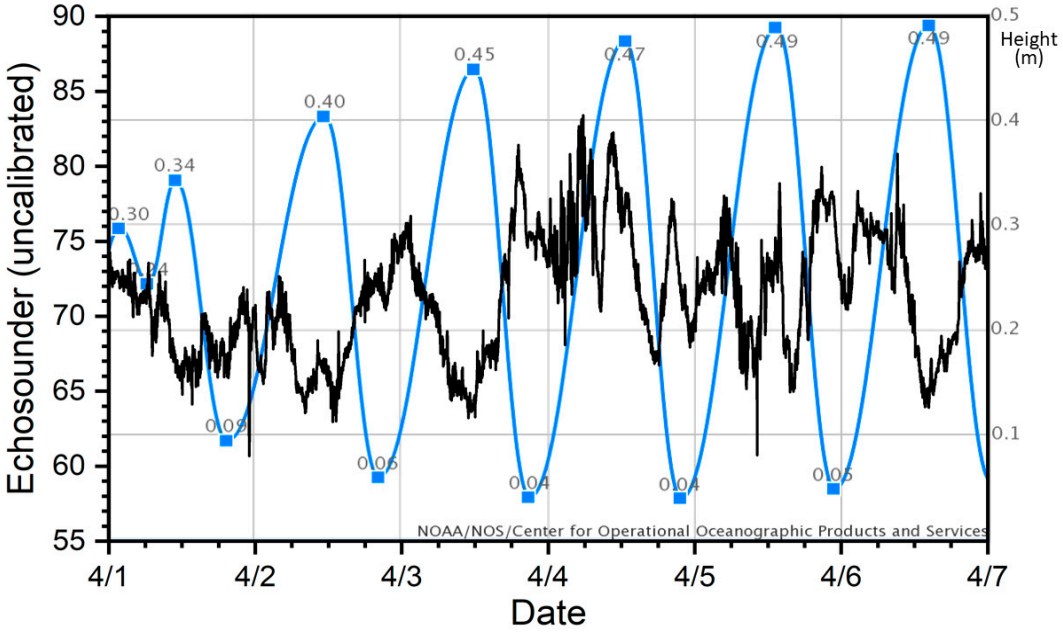

Figure 12. Bottom echo intensity data (average values over the bottom 2 m of the water column) vs. time, from the ADCP at mooring BP2. Tidal stage is indicated by the blue line (right axis, water height in m above Mean Lower-Low Water datum, from the NOAA Tides and Currents web page, Horn Island station 8742221: https://tidesandcurrents.noaa.gov/noaatidepredictions.html?id=8742221). Times indicated are local (UTC –5 h).

3.4. Model Heat Flux and Vertical Structure

COAMPS model simulations indicate a reduction in surface heat flux (cooling of surface water) between 4/3 and 4/5 (Figure 13a,b). This corresponds to the passage of a cold front from around 08:00 UTC on 4/4 to 19:00 UTC on 4/5, with a wind reversal from southerly to northerly winds, then back to southerly (Figure 2). The surface cooling in the model results is confirmed by the surface temperature decrease observed at moorings LM3 and LM4 (Figure 13c) located just seaward of the pass between Ship and Horn Islands (see mooring locations in Figure 3). A 2.5° C temperature drop is observed at both moorings over the time period between the two model heat flux fields shown in Figure 13a,b.

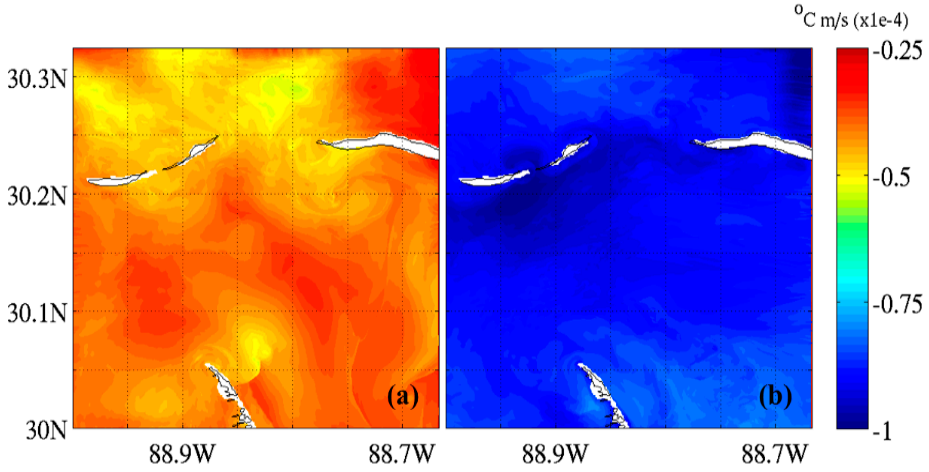

Figure 13. *Cont.*

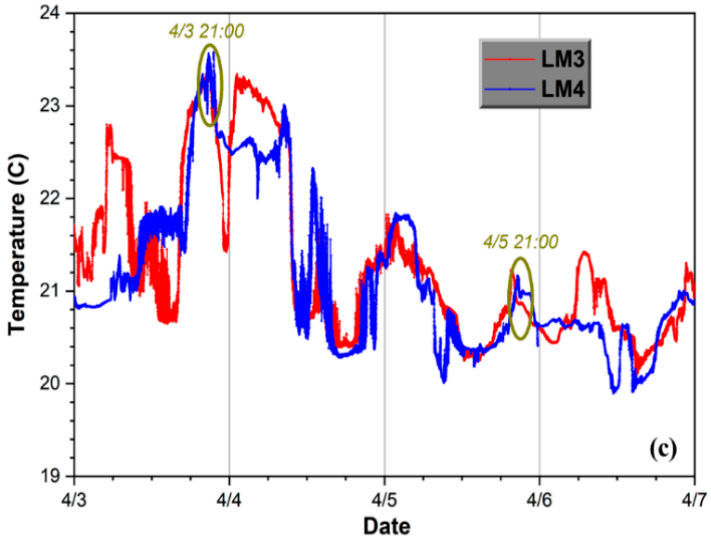

Figure 13. Model-mooring comparison. (**a**) Model temperature flux (°C m/s) at 21:00 UTC on 4/3; (**b**) Model temperature flux (°C m/s) at 21:00 UTC on 4/5; (**c**) Surface temperature (°C) at moorings LM3 and LM4 (times corresponding to model results in panels **a** and **b** are indicated).

We also analyzed model salinity predictions; Figure 14 shows surface and vertical distributions at 16:00 UTC on 4/4 and 4/5. Model surface salinity was relatively low on 4/4, with slightly higher values south of the island pass (Figure 14a). Higher model values were observed in the pass and southward on 4/5 (Figure 14b). An increase in surface salinity on 4/5 was also observed in the LM3 mooring observations (Figure 7a). Thus, both the decrease in temperature and the increase in salinity predicted by the model on 4/5 are confirmed by the mooring observations.

Vertical model sections along a longitudinal transect through the center of the pass (black line in Figure 14a) show a strong stratification at the beginning of the wind reversal on 4/4, with a well-defined two-layer system in salinity (Figure 14c). As upwelling and surface cooling continued, the two-layer system completely collapsed to well-mixed or very weakly stratified water columns in the modeling domain around the islands (Figure 14d). There is a local maximum in turbidity observed in the LM1 mooring record on 4/5 (Figure 5a) that could be related to this water column mixing event.

So, in addition to the surface cooling observed and predicted by the model, a pulse of more saline surface water was advected into the area. Thus, model surface and subsurface predictions demonstrated that there was a combination of advection of upwelled more saline water into the area, as well as mixing of the water column due to wind, surface cooling and tidal mixing. This also formed and sharpened the front observed by aircraft imagery and by ship surveys on 4/5.

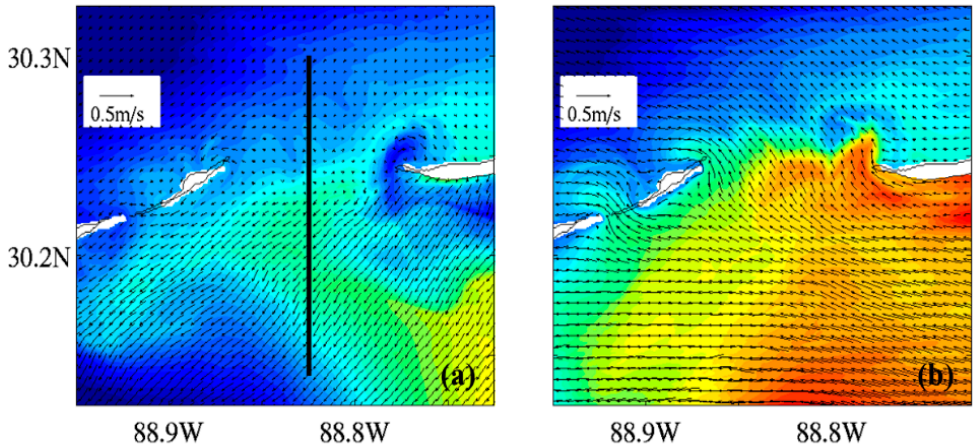

Figure 14. *Cont.*

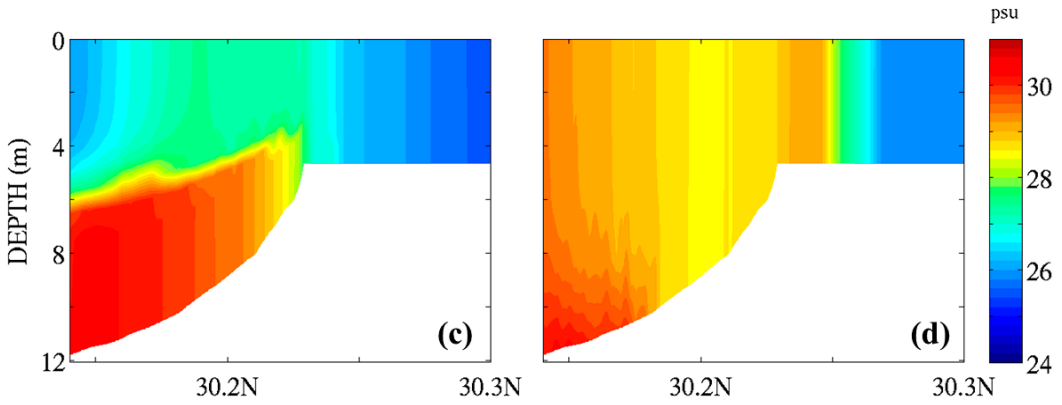

Figure 14. Model results, salinity. (**a**) Surface salinity at 1600 UTC on 4/4. Vertical black line indicates location of the vertical sections shown in panels **c** and **d**; (**b**) Surface salinity at 1600 UTC on 4/5; (**c**) Vertical salinity corresponding to date/time indicated in panel **a**; (**d**) Vertical salinity corresponding to date/time indicated in panel **b**.

4. Discussion

Atmospheric and tidal fronts are widespread, recurring forcing mechanisms in coastal zones. Knowledge of their impact on small-scale physical and bio-optical property distributions, and their accurate representation in high-resolution, predictive coastal models is crucial to achieve accurate, robust ocean forecasts in shallow coastal waters. Sub-mesoscale (0.1 to 10 km) fronts and filaments are ubiquitous features in coastal regions and their importance in coupled ocean–atmosphere processes has been recognized, yet measurements of their dynamics are rare [38]. Coincident, high-resolution remote sensing and in situ observational data sets at appropriate space/time scales to characterize very shallow coastal processes are limited. Such data sets are needed to facilitate development, parameterization, and validation of the new high-resolution coastal models.

A number of studies have been directed at larger scale processes on the continental shelf and slope. For example, the Shelf Edge Exchange Processes (SEEP) field experiment program from 1983–1989 investigated the fate of particulate matter, specifically carbon export from the shelf to the slope in the Middle Atlantic Bight [39,40]. The Sediment Transport Events on Shelves and Slopes (STRESS) program from 1989 to 1991 focused on bottom boundary layer processes on the continental shelf off northern California [41]. The Coastal Mixing and Optics (CMO) program from 1995 to 1997 looked at the mixing on a continental shelf, focusing on longer time scales (seasonal) and mesoscale shelf/slope dynamics associated with filaments, jets, and eddies [42].

Several projects have addressed aspects of coastal optics, but with sampling limitations or with different research goals. In 1994, high-resolution aircraft imagery, vertical ship profiles, and a mooring time series of physical and bio-optical measurements were collected off Fort Walton Beach, Florida, extending from the surf zone out to a water depth of approximately 10 m. The goals of that study were to assess temporal bio-optical variability, derive water bio-optical properties from the aircraft imagery, and estimate the 3D vertical optical structure of the water column by coupling the in situ measurements with the remote sensing imagery [43,44]. A modeling component was not included in that study.

The Office of Naval Research (ONR) sponsored Hyperspectral Coastal Ocean Dynamics Experiment in 2000–2001 collected an extensive suite of data at the Long-Term Ecosystem Observatory off New Jersey (LEO-15) [45]. However, the measurements were in somewhat deeper water (15–25 m vice 4–11 m in this study), there was only a single shallow bio-optical mooring (we deployed an array of eight closely-spaced moorings during ICoBOD) [10], and the focus was to examine upwelling processes along the New Jersey shore. The ocean model was also at a lower spatial resolution (300 m vice 50 m resolution for our model simulations), and the main goal of the modeling component was to develop a real-time capability for rapid environmental assessment and forecasting [46,47].

Another ONR program, Radiance in a Dynamic Ocean (RaDyO), conducted field campaigns in September, 2008 off California and Hawaii (in water depths of 170 m and 4500 m, respectively) to assess fine-scale optical variability near the ocean surface. The California site in the Santa Barbara Channel was selected as a relatively quiescent wind-wave environment and the Hawaiian site was selected for its open-ocean characteristics with high, persistent winds and large sea states. RaDyO was focused on optical variability related to underwater visibility and imaging, and on meteorological, physical, biological, and chemical processes at time and space scales as short as milliseconds and millimeters and less [48]. Thus, the project goals and environmental conditions during RaDyO were quite different from those for ICoBOD.

A small-scale, near-shore field experiment was conducted in Waimanola Bay, in February 2010 to collect physical and optical measurements to support development of an underwater visibility model [49]. The model, based on physical (waves, currents) and optical properties (backscattering, beam attenuation coefficients) and numerical wave and hydrodynamic models, provides a capability to predict the probability of object detection at a specified visibility range. However, the measurements collected during that study covered a very small area (about 200 m × 30 m) in the surf zone, thus covering a smaller, shallower area than the ICoBOD area-of-interest. In addition, measurements were only collected during daylight hours over a one-week period, so sampling limitations precluded their ability to address the impacts of tidal or atmospheric frontal passage.

Thus, due to modeling, remote sensing, and observational limitations, much of the previous coastal research has not addressed fine-scale spatial/temporal bio-optical variability in very shallow waters, nor has it specifically addressed the separate and combined impacts of atmospheric and tidal fronts on the bio-optics. To address these shortcomings, we designed a coastal field experiment that combined remote sensing with in situ ship and mooring measurements and high-resolution hydrodynamic modeling to improve understanding of coastal bio-optical variability related to atmospheric and tidal fronts. The field sampling program was designed to determine if/when a bio-optical front forms and how long it persists, in relation to the prevailing winds and the tidal stage.

We collected an extensive suite of physical and bio-optical data during a field campaign in March/April 2018 in Mississippi Sound (northern Gulf of Mexico). We also performed high-resolution (50 m) model simulations to aid interpretation of the coastal dynamics. One of the goals of the ICoBOD project is to assess bio-optical variability associated with physical forcing in the coastal environment. Our assumption, as in [41], is that robust relationships exist between the physical energy sources and optical variability in shallow coastal areas. For example, we observed increased turbidity associated with strong winds, waves, and tidal currents. We developed a relationship between turbidity and the beam attenuation coefficient at 532 nm, c(532), enabling us to subsequently estimate diver visibility, and we observed changes in diver visibility related to the passage of a high-turbidity surface plume. The strong relationship (high R^2) between c(532) and turbidity indicates that bottom resuspension was a main driver of attenuation, at least over this time period at this location. However, because particle characteristics (size and composition) affect optical properties such as c(532), additional work is needed in other areas to determine the general applicability of this relationship.

Although we did not collect bottom samples to assess sediment type, bottom-type maps from the Northern Gulf Littoral Initiative (NGLI) project in 2002 indicated a spatially heterogeneous distribution, with the pass between Ship and Horn Islands dominated by sand and the areas just north and south of the pass dominated by silts and mud (NGLI, unpublished data). In addition, recent hydrodynamic, wave, and sediment transport modeling, and geophysical surveys (including detailed sediment analyses), are available from the U.S. Army Corps of Engineers (USACE) as part of an extensive environmental assessment conducted in association with their dredging and barrier island restoration project in the Gulf Islands National Seashore (which encompasses the ICoBOD study area) [50,51]. Their analyses also indicate a very spatially heterogeneous distribution of sand, silt, and clay.

Another project goal is to examine the spatial and temporal evolution of the physical properties associated with tidal and atmospheric forcing in this coastal zone. The mooring time series allowed us

to address this aspect. We observed a warm, low salinity pulse at the surface at LM3, associated with southerly winds (Figure 7a). This seems somewhat counter-intuitive; we would expect the southerly winds to introduce higher salinity, offshore waters over the mooring. However, there is a complex interaction between the winds, tides, and currents in this area, with the currents driven mainly by the tides (see Figure 8), even though the tidal range is not large, only about 0.6 m (see Figure 2). In addition, the barrier islands seem to impart some additional spatial variability on the temperature and salinity distributions, due to the disruption of the current flow. A sharp decrease in temperature and increase in salinity was observed after this pulse.

To better understand the local processes impacting these distributions, we examined the timing of the events at finer temporal resolution. During the warm, low salinity pulse from about 1600 UTC on 4/3–0900 UTC on 4/4 (depicted by the black oval on Figure 7A), the winds are from the south for the entire period, but the currents rotate from the NW to the SE, due to the tidal shift. Thus, even though the current direction reverses, the salinity remains low. We believe that the currents from the north during ebb tide push the lower salinity water southward over the mooring (even against the southerly winds), then that low salinity water is pushed back to the north over the mooring during the initial stage of the flood tide. As the currents toward the north persist during the later flood stage, higher salinity water from farther south is eventually pushed over the mooring, even against the north winds during the initial part of the cold front passage. So, the location of convergence front seems to "slosh" back and forth at the surface over the mooring. During the cold front passage from 0800 UTC on 4/4–1900 UTC on 4/5 winds are from the north, but the currents rotate during that period due to the tides. When the wind direction is in phase with the tidal flow, current magnitudes are 2–3 times higher.

Another project goal is to examine the development, strength, duration, and decay of bottom nepheloid layers (high turbidity layers of resuspended sediment) as they relate to winds and currents. Nepheloid layers are commonly observed phenomena globally [17–19,52,53]. In the BOPPERS time series data, although the highest beam attenuation signals were observed within 4–5 m of the bottom, we also observed anomalously elevated signals extending to the surface (above background levels, related to resuspension of bottom sediments, Figure 10c). The elevated surface signals would likely be detected in a time-series of remote sensing imagery (which we did not have for this time period). It would be difficult, however, to attribute elevated turbidity values observed in an image time series to any single cause (such as tidally-generated bottom resuspension), without sufficiently fine observation frequency and long coverage (over several tidal cycles), along with collection of a concurrent time series of *in situ* vertical profiles. Anecdotally, the large internal cavity of the BOPPERS was completely filled with mud/silt after the 25-day deployment, the weight of which caused the rope line to break twice during recovery. These fine-grain bottom sediments were likely easily resuspended by bottom currents, leading to nepheloid layer development. Due to the widespread observation (temporally and spatially) of nepheloid layers in this area, they likely contribute significantly to regional sediment transport.

Atmospheric cold fronts in the northern Gulf of Mexico can significantly impact the coastal environment, including coastline morphology through depositional and erosion processes, sediment concentration and transport, water temperature, heat flux and energy balance, wave action, circulation, and the exchange of coastal and offshore waters. It has been suggested that due their regular frequency and large area of coverage, their impact can be cumulative and more significant than the passage of an occasional tropical storm [54]. Observations and modeling studies in the Gulf of Mexico have demonstrated the effect of the cold air outbreaks on the hydrography and biology of Shelf waters [55–58], and on the bio-optical properties of coastal waters [59,60]. They are common occurrences in the spring in Mississippi Sound, and during the course of our 25-day field experiment, four cold fronts passed through. The model simulations captured their impact on the study area; heat flux and salinity fields clearly revealed the cooling and mixing of the water column over two days, and these predictions were confirmed by the in situ mooring observations.

The model can also help us address several related scientific questions: What are the relative contributions of tidal and atmospheric processes to front formation? Are submesoscale processes

(like surface frontogenesis) also responsible for the front formation? However, it is challenging to conduct a COAMPS 50 m model run with tidal forcing turned off, because the COAMPS 50 m domain is triply nested in other Gulf of Mexico (GOM) submodels, which all have tidal forcing. We would have to rerun all GOM nests with tides turned off. Instead, to help answer these questions, we are repeating the baseline 50 m model run (which includes tidal and atmospheric forcing) with simulations where we selectively turn of all atmospheric forcing (which will allow us to assess tidal effects), just winds, or just heat flux (to asses surface heating). These additional model runs (currently underway) will enable us to partition the various forcing effects to better understand frontal dynamics.

5. Conclusions

Time series of temperature, salinity, waves, currents, and turbidity data sets collected by multiple moorings demonstrated temporal variability related to tides and winds, with differences observed between the surface and bottom layers even in these shallow waters (11 m depths and less). We developed a relationship to estimate beam attenuation at 532 nm, c(532), from the turbidity measurements (in NTU). We then applied an existing relationship to calculate diver visibility from the c(532) values. The conversion from turbidity to c(532) enabled us to spatially extend the visibility data set (because we had measurements of turbidity at more locations than we had c(532) measurements. A short, intense turbidity pulse unrelated to the tides or bottom resuspension was observed in the time series at one of the moorings; it was also captured in the time-lapse record of an underwater camera, which provided us with a visual reference for the turbidity measurements.

Using the data from the profiling mooring, we related nepheloid layer development and decay, and vertical extent into the water column, to bottom currents and tidal stage. The observed nepheloid layer developed around slack tide prior to flood stage, lasted about 9–12 h, and the main turbidity signal extended about 4–5 m above the bottom (roughly half of the water column), although anomalously elevated values were observed all the way to the surface.

High-resolution (50 m) coupled ocean–atmosphere model simulations predicted a decrease is surface heat flux over a 2-day period associated with the passage of a cold front with strong northerly winds. Mooring temperature and salinity measurements confirmed the model-predicted surface cooling and salinity increase. Additional model runs with various forcing processes turned on/off are underway, and will enable us to better separate the individual effects of tides, winds and heat flux on the physical and bio-optical property distributions.

Author Contributions: Conceptualization, R.W.G.J.; methodology, R.W.G.J., M.D.L., W.D.M., I.S., G.B.S., T.A.S., H.W.W.; investigation, R.W.G.J., M.D.L., W.D.M., G.B.S., H.W.W.; formal analysis, all.; validation, S.A., I.S., T.A.S., D.W.W.; software, S.A., M.D.L., W.D.M., I.S., T.A.S., D.W.W.; visualization, all; writing—original draft preparation, R.W.G.J.; writing—review and editing, all; project administration. R.W.G.J.; funding acquisition, R.W.G.J. All authors have read and agreed to the published version of the manuscript.

Funding: This research was funded by the Naval Research Laboratory project, Integrated Coastal Bio-Optical Dynamics: Impact of Atmospheric and Tidal Fronts (Program Element 61153N).

Acknowledgments: We thanks Ian Martens, Andrew Quaid, Wesley Goode, and Joel Wesson for invaluable assistance with instrumentation and data collection. We also thank the captains and crews of the R/V Point Sur and the R/V Wilson for their support during the field operations, and Sky Andrew, Matt Wallace, and Marcus Apple (PrecisionHawk, Inc.) for collection of the UAV imagery.

Conflicts of Interest: The authors declare no conflict of interest. The funders had no role in the design of the study; in the collection, analyses, or interpretation of data; in the writing of the manuscript, or in the decision to publish the results.

References

1. Mobley, C.D. *Light and Water: Radiative Transfer in Natural Waters*; Academic: New York, NY, USA, 1994; p. 592.
2. Mascarenhas, V.; Keck, T. Marine Optics and Ocean Color Remote Sensing. In Proceedings of the YOUMARES 8—Oceans Across Boundaries: Learning from Each Other, Kiel, Germany, 13–15 September 2017; pp. 41–54.

3. Kirk, J.T. *Light and Photosynthesis in Aquatic Ecosystems*; Cambridge University Press: Cambridge, UK, 1994; p. 509.
4. Falkowski, P.G.; Raven, J.A. *Aquatic Photosynthesis*; Princeton University Press: Princeton, NJ, USA, 2007; p. 483.
5. Zhang, Y.; Liu, M.; Qin, B.; Feng, S. Photochemical degradation of chromophoric-dissolved organic matter exposed to simulated UV-B and natural solar radiation. *Hydrobiologia* **2009**, *627*, 159–168. [CrossRef]
6. Vodacek, A.; Blough, N.V.; DeGrandpre, M.D.; DeGrandpre, M.D.; Nelson, R.K. Seasonal variation of CDOM and DOC in the Middle Atlantic Bight: Terrestrial inputs and photooxidation. *Limnol. Oceanogr.* **1997**, *42*, 674–686. [CrossRef]
7. Werdell, P.J.; McKinna, L.I.W.; Boss, E.; Ackleson, S.G.; Craig, S.E.; Gregg, W.W.; Lee, Z.; Maritorena, S.; Roesler, C.S.; Rousseaux, C.S.; et al. An overview of approaches and challenges for retrieving marine inherent optical properties from ocean color remote sensing. *Prog. Oceanogr.* **2018**, *160*, 186–212. [CrossRef] [PubMed]
8. Yoder, J.A.; McClain, C.R.; Blanton, J.O.; Oeymay, L.Y. Spatial scales in CZCS-chlorophyll imagery of the southeastern US continental shelf. *Limnol. Oceanogr.* **1987**, *32*, 929–941. [CrossRef]
9. Denman, K.L.; Abbott, M.R. Time evolution of surface chlorophyll patterns from cross-spectrum analysis of satellite color images. *J. Geophys. Res. Oceans* **1988**, *93*, 6789–6798. [CrossRef]
10. Chang, G.C.; Dickey, T.D.; Schofield, O.M.; Weidemann, A.D.; Boss, E.; Pegau, W.S.; Moline, M.A.; Glenn, S.M. Nearshore physical processes and bio-optical properties in the New York Bight. *J. Geophys. Res. Oceans* **2002**, *107*, 16-1–16-16. [CrossRef]
11. Babin, M.; Stramski, D.; Ferrari, G.M.; Claustre, H.; Bricaud, A.; Obolensky, G.; Hoepffner, N. Variations in the light absorption coefficients of phytoplankton, nonalgal particles, and dissolved organic matter in coastal waters around Europe. *J. Geophys. Res. Oceans* **2003**, *108*. [CrossRef]
12. Vantrepotte, V.; Brunet, C.; Mériaux, X.; Lécuyer, E.; Vellucci, V.; Santer, R. Bio-optical properties of coastal waters in the Eastern English Channel. *Estuar. Coast. Shelf Sci.* **2007**, *72*, 201–212. [CrossRef]
13. Henry, W.K. Some Aspects of the Fate of Cold Fronts in the Gulf of Mexico. *Mon. Weather Rev.* **1979**, *107*, 1078–1082. [CrossRef]
14. Riddick, C.A.L.; Hunter, P.D.; Tyler, A.N.; Martinez-Vicente, V.; Horváth, H.; Kovács, A.W.; Vörös, L.; Preston, T.; Présing, M. Spatial variability of absorption coefficients over a biogeochemical gradient in a large and optically complex shallow lake. *J. Geophys. Res. Oceans* **2015**, *120*, 7040–7066. [CrossRef]
15. Zhang, Y.; Qin, B.; Zhu, G.; Gao, G.; Luo, L.; Chen, W. Effect of sediment resuspension on underwater light field in shallow lakes in the middle and lower reaches of the Yangtze River: A case study in Longgan Lake and Taihu Lake. *Sci. China Ser. D* **2006**, *49*, 114–125. [CrossRef]
16. Liu, X.; Zhang, Y.; Wang, M.; Zhou, Y. High-frequency optical measurements in shallow Lake Taihu, China: Determining the relationships between hydrodynamic processes and inherent optical properties. *Hydrobiologia* **2014**, *724*, 187–201. [CrossRef]
17. Smart, J.H. How accurately can we predict optical clarity in the littorals? *Johns Hopkins Appl. Tech. Dig.* **2004**, *25*, 112–120.
18. Ziervogel, K.; Dike, C.; Asper, V.; Montoya, J.; Battles, J.; D'souza, N.; Passow, U.; Diercks, A.; Esch, M.; Joye, S.; et al. Enhanced particle fluxes and heterotrophic bacterial activities in Gulf of Mexico bottom waters following storm-induced sediment resuspension. *Deep Sea Res. Part II Top. Stud. Oceanogr.* **2016**. [CrossRef]
19. Johnson, D.R.; Weidemann, A.; Pegau, W.S. Internal tidal bores and bottom nepheloid layers. *Cont. Shelf Res.* **2001**, *21*, 1473–1484. [CrossRef]
20. Pineda, J. Internal tidal bores in the nearshore: Warm-water fronts, seaward gravity currents and the onshore transport of neustonic larvae. *J. Mar. Res.* **1994**, *52*, 427–458. [CrossRef]
21. Reeves, A.D.; Duck, R.W. Density fronts: Sieves in the estuarine sediment transfer system? *Phys. Chem. Earth Part B Hydrol. Oceans Atmos.* **2001**, *26*, 89–92. [CrossRef]
22. Hodur, R.M. The Naval Research Laboratory's coupled ocean/atmosphere mesoscale prediction system (COAMPS). *Mon. Weather Rev.* **1997**, *125*, 1414–1430. [CrossRef]
23. Chen, S.; Cummings, J.; Doyle, J.; Hodur, R.; Holt, T.; Liou, C.S.; Liu, M.; Mirin, A.; Ridout, J.; Schmidt, J.; et al. *COAMPS Version 3 Model Description—General Theory and Equations*; NRL/PU/7500–04–488; Naval Research Laboratory: Washington, DC, USA, 2003; p. 141.

24. Small, R.J.; Carniel, S.; Campbell, T.; Teixeira, J.; Allard, R. The response of the Ligurian and Tyrrhenian Seas to a summer Mistral event: A coupled atmosphere–ocean approach. *Oceans Model.* **2012**, *48*, 30–44. [CrossRef]
25. Gould, R.W.; Book, J.W.; Hulbert, M.S.; Quaid, A.J.; Smith, R.H.; Hughes, E.W.; McCormick, B.L.; McNeal, D.N.; Harrington, J.C. System and Method for Bio-Optical Environmental Reconnaissance. U.S. Patent US9501450B2, 22 November 2016.
26. Smith, T.A.; Jolliff, J.K.; Walker, N.D.; Anderson, S. Biophysical Submesoscale Processes in the Wake of Hurricane Ivan: Simulations and Satellite Observations. *J. Mar. Sci. Eng.* **2019**, *7*, 378. [CrossRef]
27. Daley, R.; Barker, E. NAVDAS: Formulation and Diagnostics. *Mon. Weather Rev.* **2001**, *129*, 869–883. [CrossRef]
28. Martin, P.J. *Description of the Navy Coastal Ocean Model Version 1.0*; NRL/FR/732–0-9962; Naval Research Laboratory: Washington, DC, USA; Stennis Space Center: Hancock County, MS, USA, 2000.
29. Booij, N.; Ris, R.C.; Holthuijsen, L.H. A third-generation wave model for coastal regions: 1. Model description and validation. *J. Geophys. Res. Oceans* **1999**, *104*, 7649–7666. [CrossRef]
30. Tolman, H.L. *User Manual and System Documentation of WAVEWATCH III Version 4.18*; NOAA/NWS/NCEP: College Park, MD, USA, 2014; p. 311.
31. Collins, N.; Theurich, G.; DeLuca, C.; Suarez, M.; Trayanov, A.; Balaji, V.; Li, P.; Yang, W.; Hill, C.; da Silva, A. Design and Implementation of Components in the Earth System Modeling Framework. *Int. J. High Perform. Comput. Appl.* **2005**, *19*, 341–350. [CrossRef]
32. Hogan, T.F.; Liu, M.; Ridout, J.A.; Peng, M.S.; Whitcomb, T.R.; Ruston, B.C.; Reynolds, C.A.; Eckermann, S.D.; Moskaitis, J.R.; Baker, N.L. The navy global environmental model. *Oceanography* **2014**, *27*, 116–125. [CrossRef]
33. Metzger, E.J.; Helber, R.W.; Hogan, P.J.; Posey, P.G.; Thoppil, P.G.; Townsend, T.L.; Wallcraft, A.J. *Global Ocean. Forecast. System 3.1 Validation Testing*; Naval Research Laboratory: Washington, DC, USA; Stennis Space Center: Hancock County, MS, USA, 2017.
34. Fox, D.N.; Barron, C.N.; Carnes, M.R.; Booda, M.; Peggion, G.; Van Gurley, J. The Modular Ocean Data Assimilation System. *Oceanography* **2002**, *15*, 22–28. [CrossRef]
35. Cummings, J.A. Operational multivariate ocean data assimilation. *Q. J. R. Meteor. Soc.* **2005**, *131*, 3583–3604. [CrossRef]
36. Zaneveld, J.R.; Pegau, W. Robust underwater visibility parameter. *Opt. Express* **2003**, *11*, 2997–3009. [CrossRef]
37. Gostiaux, L.; van Haren, H. Extracting Meaningful Information from Uncalibrated Backscattered Echo Intensity Data. *J. Atmos. Oceans Technol.* **2010**, *27*, 943–949. [CrossRef]
38. Gommenginger, C.; Chapron, B.; Hogg, A.; Buckingham, C.; Fox-Kemper, B.; Eriksson, L.; Soulat, F.; Ubelmann, C.; Ocampo-Torres, F.; Nardelli, B.B.; et al. SEASTAR: A Mission to Study Ocean Submesoscale Dynamics and Small-Scale Atmosphere-Ocean Processes in Coastal, Shelf and Polar Seas. *Front. Mar. Sci.* **2019**, 6. [CrossRef]
39. Biscaye, P.E.; Anderson, R.F.; Deck, B.L. Fluxes of particles and constituents to the eastern United States continental slope and rise: SEEP—I. *Cont. Shelf Res.* **1988**, *8*, 855–904. [CrossRef]
40. Biscaye, P.E.; Flagg, C.N.; Falkowski, P.G. The shelf edge exchange processes experiment, SEEP-II: An introduction to hypotheses, results and conclusions. *Deep Sea Res. Part II Top. Stud. Oceanogr.* **1994**, *41*, 231–252. [CrossRef]
41. Trowbridge, J.H.; Nowell, A.R.M. An introduction to the Sediment TRansport Events on Shelves and Slopes (STRESS) program. *Cont. Shelf Res.* **1994**, *14*, 1057–1061. [CrossRef]
42. Dickey, T.D.; Williams, A.J., III. Interdisciplinary ocean process studies on the New England shelf. *J. Geophys. Res. Oceans* **2001**, *106*, 9427–9434. [CrossRef]
43. Gould, R.W.; Arnone, R.A. Remote sensing estimates of inherent optical properties in a coastal environment. *Remote Sens. Environ.* **1997**, *61*, 290–301. [CrossRef]
44. Gould, R.W.; Arnone, R.A. Three-dimensional modelling of inherent optical properties in a coastal environment: Coupling ocean colour imagery and in situ measurements. *Int. J. Remote Sens.* **1998**, *19*, 2141–2159. [CrossRef]
45. Dickey, T.D. Studies of Coastal Ocean Dynamics and Processes Using Emerging Optical Technologies. *Oceanography* **2004**, *17*, 9–13. [CrossRef]

46. Schofield, O.; Bergmann, T.; Bissett, P.; Grassle, J.F.; Haidvogel, D.B.; Kohut, J.; Moline, M.; Glenn, S.M. The Long-term Ecosystem Observatory: An integrated coastal observatory. *IEEE J. Oceans Eng.* **2002**, *27*, 146–154. [CrossRef]
47. Wilkin, J.L.; Arango, H.G.; Haidvogel, D.B.; Lichtenwalner, C.S.; Glenn, S.M.; Hedström, K.S. A regional ocean modeling system for the Long-term Ecosystem Observatory. *J. Geophys. Res. Oceans* **2005**, *110*. [CrossRef]
48. Dickey, T.; Banner, M.L.; Bhandari, P.; Boyd, T.; Carvalho, L.; Chang, G.; Chao, Y.; Czerski, H.; Darecki, M.; Dong, C.; et al. Introduction to special section on Recent Advances in the Study of Optical Variability in the Near-Surface and Upper Ocean. *J. Geophys. Res. Oceans* **2012**, *117*. [CrossRef]
49. Chang, G.; Jones, C.; Twardowski, M. Prediction of optical variability in dynamic nearshore environments. *Methods Oceanogr.* **2013**, *7*, 63–78. [CrossRef]
50. Wamsley, T.V.; Godsey, E.S.; Bunch, B.W.; Chapman, R.S.; Gravens, M.B.; Grzegorzewski, A.S.; Johnson, B.D.; King, D.B.; Permenter, R.L.; Tillman, D.H.; et al. *Mississippi Coastal Improvements Program; Evaluation of Barrier Island Restoration Efforts*; ERDC TR-13-12; U.S. Army Corps of Engineers, Engineer Research and Development Center: Vicksburg, MS, USA, 2013.
51. FitzHarris, M.; Godsey, E. *Mississippi Coastal Improvements Program, Barrier Island Restoration Project, Offshore Sand Borrow Investigation, 2010–2014: Geotechnical Engineering Report*; U.S. Army Corps of Engineers: Washington, DC, USA, 2015.
52. Hoge, F.E.; Wright, C.W.; Krabill, W.B.; Buntzen, R.R.; Gilbert, G.D.; Swift, R.N.; Yungel, J.K.; Berry, R.E. Airborne lidar detection of subsurface oceanic scattering layers. *Appl. Opt.* **1988**, *27*, 3969–3977. [CrossRef] [PubMed]
53. Verspecht, F.; Pattiaratchi, C. On the significance of wind event frequency for particulate resuspension and light attenuation in coastal waters. *Cont. Shelf Res.* **2010**, *30*, 1971–1982. [CrossRef]
54. Moeller, C.C.; Huh, O.K.; Roberts, H.H.; Gumley, L.E.; Menzel, W.P. Response of Louisiana coastal environments to a cold front passage. *J. Coast. Res.* **1993**, 434–447.
55. Huh, O.K.; Rouse, L.J., Jr.; Walker, N.D. Cold air outbreaks over the northwest Florida continental shelf: Heat flux processes and hydrographic changes. *J. Geophys. Res. Oceans* **1984**, *89*, 717–726. [CrossRef]
56. Nowlin, W.D., Jr.; Parker, C.A. Effects of a Cold-Air Outbreak on Shelf Waters of the Gulf of Mexico. *J. Phys. Oceanogr.* **1974**, *4*, 467–486. [CrossRef]
57. Dagg, M.J. Physical and biological responses to the passage of a winter storm in the coastal and inner shelf waters of the northern Gulf of Mexico. *Cont. Shelf Res.* **1988**, *8*, 167–178. [CrossRef]
58. Villanueva, E.E.; Mendoza, V.M.; Adem, J. Sea surface temperature and mixed layer depth changes due to cold-air outbreak in the Gulf of Mexico. *Atmofera* **2010**, *23*, 325–346.
59. Joshi, I.; D'Sa, E. Seasonal Variation of Colored Dissolved Organic Matter in Barataria Bay, Louisiana, Using Combined Landsat and Field Data. *Remote Sens.* **2015**, *7*, 12478. [CrossRef]
60. D'Sa, E.J.; Miller, R.L.; Del Castillo, C. Bio-optical properties and ocean color algorithms for coastal waters influenced by the Mississippi River during a cold front. *Appl. Opt.* **2006**, *45*, 7410–7428. [CrossRef]